Letter

Trion-trion annihilation in monolayer WS_2

Suman Chatterjee,[1] Garima Gupta,[1] Sarthak Das,[1] Kenji Watanabe,[2] Takashi Taniguchi,[3] and Kausik Majumdar[1,*]

[1]*Department of Electrical Communication Engineering, Indian Institute of Science, Bangalore 560012, India*

[2]*Research Center for Functional Materials, National Institute for Materials Science, 1-1 Namiki, Tsukuba 305-044, Japan*

[3]*International Center for Materials Nanoarchitectonics, National Institute for Materials Science, 1-1 Namiki, Tsukuba 305-044, Japan*

(Received 14 October 2021; revised 26 February 2022; accepted 9 March 2022; published 28 March 2022)

Strong Coulomb interaction in monolayer transition metal dichalcogenides can facilitate nontrivial many-body effects among excitonic complexes. Many-body effects such as exciton-exciton annihilation have been widely explored in this material system. However, a similar effect for charged excitons (or trions), that is, trion-trion annihilation (TTA), is expected to be relatively suppressed due to repulsive like-charges, and it has not been hitherto observed in such layered semiconductors. By a gate-dependent tuning of the spectral overlap between the trion and the charged biexciton through an "anticrossing"-like behavior in monolayer WS_2, here we present an experimental observation of an anomalous suppression of the trion emission intensity with an increase in gate voltage. The results strongly correlate with time-resolved measurements, and they are inferred as direct evidence of a nontrivial TTA resulting from nonradiative Auger recombination of a bright trion, and the corresponding energy resonantly promoting a dark trion to a charged biexciton state. The extracted Auger coefficient for the process is found to be tunable ten-fold through a gate-dependent tuning of the spectral overlap.

DOI: 10.1103/PhysRevB.105.L121409

I. INTRODUCTION

Semiconducting monolayers of transition metal dichalcogenides (TMDCs) exhibit strongly bound excitons and other higher-order excitonic complexes [1–9]. Under high excitation density, large Coulomb interaction in these sub-nanometer-thick monolayers can lead to a strong interaction among these excitonic complexes [3,10–15]. Among several many-body effects, exciton-exciton annihilation (EEA) in particular, as determined by the Auger interaction between two excitons, has drawn a lot of attention from researchers [10,11,13,16–18]. In a typical Auger process in bulk semiconductors (such as Si or Ge), the recombination energy of two quasiparticles (electron and hole) is taken up by a second electron, and it is promoted to a higher energy state [19–21]. The excitonic Auger process involves two excitons where one recombines nonradiatively, providing the recombination energy to a second exciton. This energy usually ionizes the receiving exciton [10,11,16]. Since these processes directly affect the quantum efficiency of optical devices [19,22], a clear understanding of such processes is of the utmost importance. On the other hand, Auger interaction can also be used to produce useful photocurrent through the generation of hot carriers [12,13].

One of the essential advantages of monolayer TMDCs lies in the gate tunability of the optical response. Under gating, the neutral exciton can easily transfer its oscillator strength to a charged exciton (or trion). Similar many-body effects such as trion-trion annihilation (TTA) should be intriguing since, on the one hand, the relatively larger Bohr radius of trions may enhance the Auger process. In contrast, on the other hand, trion-trion repulsion due to like-charges would suppress such interaction. While Auger processes in higher-order excitonic complexes have been demonstrated in quantum dots [23], no such TTA effect has been reported to date in monolayer TMDCs. In this work, we present an experimental observation of the same in gated monolayer WS_2.

II. RESULTS AND DISCUSSIONS

We prepare a stack of 1L-WS_2/hBN/few-layer graphene on a heavily doped Si wafer covered with 285 nm SiO_2 using the dry transfer method. The stack is then annealed in high vacuum at 200 °C for 3 h (see the Methods section for sample preparation). A gate voltage (V_g) is applied to the top graphene electrode while connecting 1L-WS_2 to a grounded few-layer graphene contact. The device configuration is schematically depicted in Fig. 1(a). According to previous reports [16,18], 1L-WS_2 on Si/SiO_2 exhibits an enhanced Auger effect due to localization of excitonic species. In this work, we thus intentionally keep the 1L-WS_2 flake directly on the Si/SiO_2 substrate [only covered by the top hBN; see Fig. 1(a)] to achieve an overall higher Auger rate constant [16]. All measurements are performed in an optical cryostat at $T = 5$ K unless otherwise mentioned. We excite the sample with a pulsed laser (531 nm) and collect both steady-state photoluminescence (PL) and time-resolved photoluminescence (TRPL) *in situ* (see Fig. 1 in Supplemental Material [24] for a setup schematic) at different V_g.

The spectral evolution of different excitonic peaks with V_g is depicted in a color plot in Fig. 1(b) (all the individual spectra are shown in Fig. 2 of Supplemental Material [24]). Figure 1(c) shows the respective fitted peak positions. We

*Corresponding author: kausikm@iisc.ac.in

 ©2022 American Physical Society

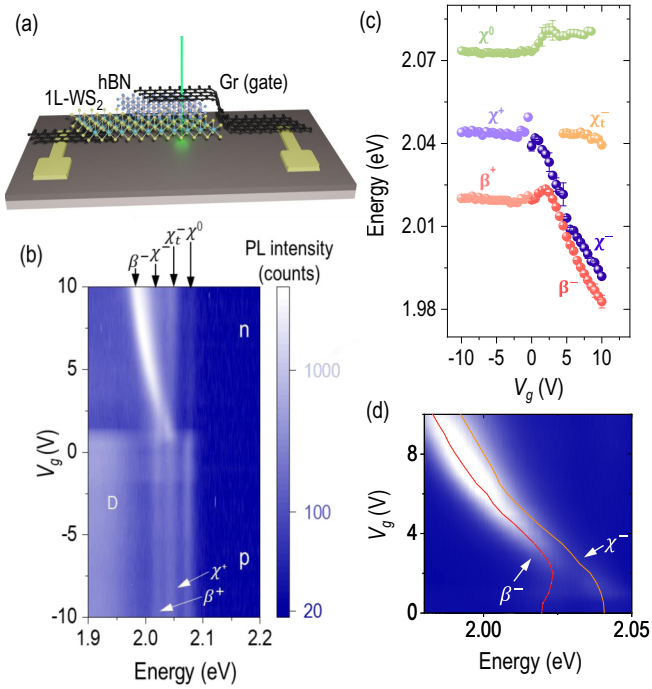

FIG. 1. Gate voltage-dependent modulation of excitonic complexes in WS_2. (a) Schematic of 1 L WS_2/hBN/few-layer graphene device. A gate voltage (V_g) is applied between the two contact pads. (b) Color plot of V_g-dependent PL intensity (in log scale) and the spectral position variation of the neutral exciton (χ^0), positive and negative trions ($\chi^{\pm}$), intervalley trion (χ_t^-), and positive and negative charged biexcitons ($\beta^{\pm}$). *p*-doping and *n*-doping regions are marked. D stands for the broad defect bound exciton emission peak. (c) Fitted peak positions of all the relevant peaks plotted as a function of V_g. The error bars obtained from multiple fits are indicated. (d) Zoomed-in portion (marked by a white dashed box) of the color plot (a), plotted in linear scale, depicting (red and yellow lines to guide the eye represent trion and biexciton, respectively) "anticrossing"-like behavior between χ^- and β^-.

explain the origin of such a nonmonotonic feature from a combination of three competing effects: (i) V_g induces charge carriers in the monolayer, the resulting screening weakens the Coulomb interaction causing a suppression of the binding energy of the excitonic complexes, which in turn results in a blueshift in the emission energy [25–27]; (ii) the vertical gate field induces a spatial separation between the electrons and holes in the excitonic complexes, leading to a suppression in the binding energy, and hence a blueshift in the emission energy [28]; and (iii) doping-induced Pauli blocking, leading to a redshift in emission [1,29–31]. The last effect is the strongest one in our sample, as explained later in more detail.

The *p*-doping side ($V_g < 0$ V) shows three distinct features [Figs. 1(b) and 1(c)], namely a neutral bright exciton (χ^0), a positive trion (χ^+), and a positively charged biexciton (β^+). Due to the relative positions of the Fermi levels between 1L-WS_2 and graphene, it is more difficult to inject holes than electrons [32]. Thus it is challenging to dope the 1L-WS_2 flake strongly *p*-type, as suggested by the sustained χ^0 peak intensity even at high negative V_g [Fig. 1(b)]. The inability to strongly dope the WS_2 film *p*-type leads to a negligible doping-induced spectral-shift of the peaks for $V_g < 0$ [as effects (i) and (iii) are negligible]. In contrast, we observe a small blueshift (about 2–4 meV) for all three peaks, shown in Fig. 3 of Supplemental Material [24]. In the absence of a significant *p*-doping, such a blueshift provides an estimate for the reduction in the binding energy due to gate-field-induced spatial separation of the electron and hole in an excitonic complex [28].

The spectral features are rich in the *n*-doping side ($V_g > 0$ V). With an increase in doping density, the χ^0 peak gradually fades out due to a transfer of its oscillator strength to the negatively charged trion (χ^-) [1,2,33–35] and charged biexciton (β^-), as indicated in Fig. 1(b). The biexcitonic nature of the β^- peak is identified through a superlinear power law [4,8,36] (see Fig. 4 of Supplemental Material [24]). While all three peaks show a slight blueshift at low positive V_g, with an increase in voltage, both the χ^- (for $V_g > 1$ V) and β^- (for $V_g > 2.5$ V) peaks exhibit a strong redshift [zoomed in Fig. 1(d)]. On the other hand, the χ^0 peak position remains nearly unaltered after an initial blueshift [Fig. 1(c)].

After $V_g > 4.5$ V, another distinct trion peak emerges around 2.04 eV—in a spectral position similar to that of χ^+ [Fig. 1(c)]. We attribute this to the formation of a negative intervalley trion (χ_t^-) from the top of the spin-split conduction bands at high V_g, as shown in Fig. 5 of Supplemental Material [24]. It appears after a certain threshold value of V_g (4.5 V) due to a lower filling of the top conduction bands. This peak shows a negligible redshift due to weak Pauli blocking at higher energy unless V_g is very high (>8 V).

As indicated in Figs. 2(a) and 2(b), the emission energy of the χ^- (β^-) peak corresponds to the transition from the trion (charged biexciton) band to the electron (trion) band. Consequently, the trion or the charged biexciton with a large center-of-mass (COM) momentum can emit a photon. This is in stark contrast with the case of a neutral exciton, where the conservation of linear momentum during radiative recombination allows only near-zero momentum states (within the light cone [37]) to emit a photon. As shown in Fig. 2(a), for the trion, as V_g increases, smaller momentum states are filled in the conduction band, and hence the trions with small momentum are not allowed to recombine due to Pauli blocking of the final state. Hence, as V_g increases, the allowed trion emission moves to a higher momentum. This effect, in turn, results in a reduction in the trion emission energy due to the different curvatures of the two participating bands. The corresponding redshift $\Delta(V_g) = \hbar\omega(V_g = 0) - \hbar\omega(V_g)$ can be directly mapped to the momentum ($\hbar Q$) of the emitting trion following the equation

$$\Delta(V_g) = \frac{\hbar^2 Q^2}{2}\left(\frac{1}{m_1} - \frac{1}{m_3}\right). \quad (1)$$

In the above equation, we neglect any minor blueshift due to screening and field effect. We also assume that there is negligible filling in the conduction band (CB) around $V_g = 0$, thus $V_g = 0$ corresponds to transitions at $Q = 0$ [shown in Fig. 2(a)]. m_1 and m_3 are the conduction-band effective mass and the center of mass of the trion, respectively.

Similarly, the charged biexciton emission moves to a larger momentum with an increase in V_g due to Pauli blocking for

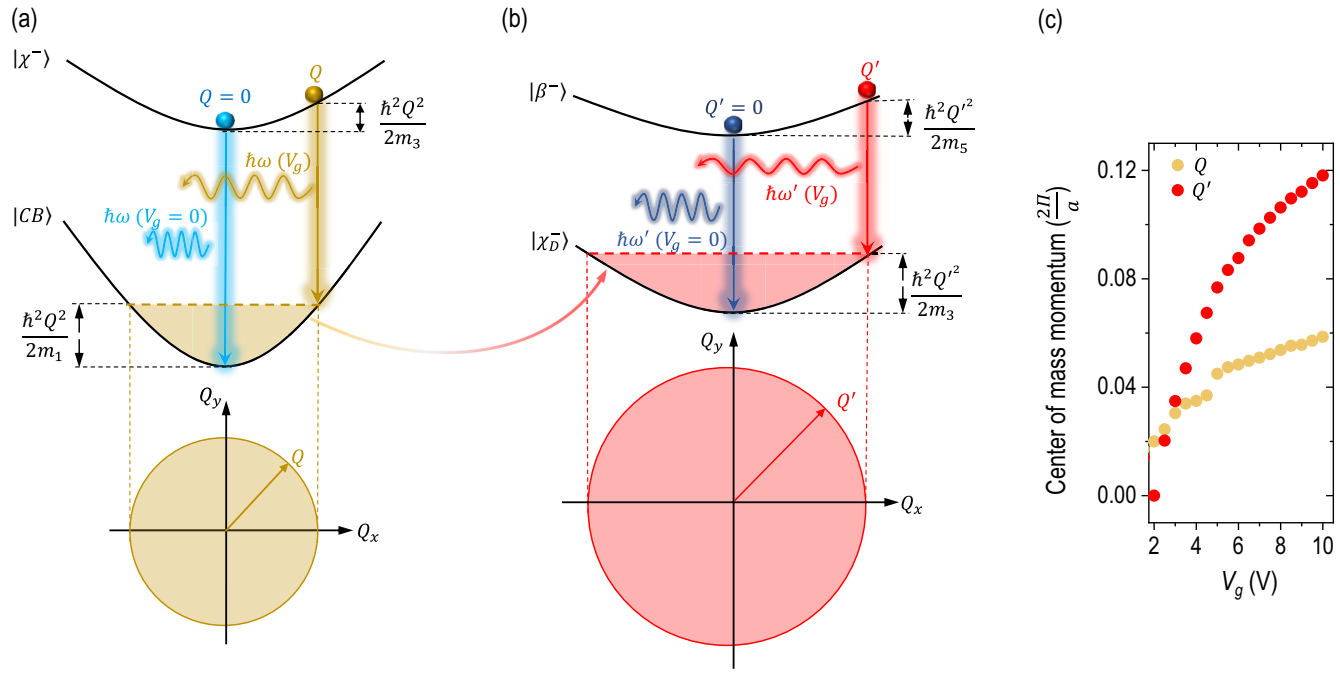

FIG. 2. Mechanism for gate-dependent redshift in emission from trion and charged biexciton with nonzero center-of-mass momenta. (a) The vertical transition from the negative trion state ($|\chi^-\rangle$) to the conduction band ($|\text{CB}\rangle$), emitting one photon, is shown at two different V_g values. At $V_g = 0$ V, $|\text{CB}\rangle$ is almost empty, and transition from the bottom of the $|\chi^-\rangle$ to $|\text{CB}\rangle$ ($Q = 0$) is possible (shown by a sky-blue arrow). With increasing n-doping ($V_g > 0$ V), lower energy $|\text{CB}\rangle$ states are blocked, and the vertical transition occurs at a higher Q value (shown by a yellow arrow). In-plane (Q_x-Q_y) slice shows filling of bands up to a radius of Q by the yellow shaded area (bottom panel). The dissimilar curvatures of the two bands result in a redshift in emission at larger filling. (b) The vertical transition from the negatively charged biexciton state ($|\beta^-\rangle$) to the dark trion ($|\chi_D^-\rangle$) state, emitting one photon at two different V_g values. $V_g = 0$ V transition occurs at $Q' = 0$ (shown by a dark blue arrow). At finite V_g, the $|\chi_D^-\rangle$ state is blocked up to Q', pushing the vertical transition to occur at higher Q' (shown by a red arrow). In-plane (Q_x-Q_y) slice area, shaded in red, indicates a larger filling compared to (a) (bottom panel). Loss of electrons from the conduction band in order to form χ_D^- is represented by a shaded arrow from $|CB\rangle$ to $|\chi_D^-\rangle$. (c) COM momenta of the emitting χ^- and β^- species plotted as a function of V_g indicating a crossover at higher V_g.

the final trion state, and results in a similar redshift due to the difference in curvature between the charged biexciton and trion bands. The COM momentum $\hbar Q'$ of the emitting charged biexciton is related to the corresponding redshift $[\Delta'(V_g) = \hbar\omega'(V_g = 0) - \hbar\omega'(V_g)]$ as

$$\Delta'(V_g) = \frac{\hbar^2 Q'^2}{2}\left(\frac{1}{m_3} - \frac{1}{m_5}\right), \tag{2}$$

where m_5 is the mass of the charged biexciton.

Using Eqs. (1) and (2), in Fig. 2(c) we plot the extracted Q and Q' from the measured redshifts in Fig. 1(c) as a function of V_g. One striking observation is that, for $V_g > 2.5$ V, Q' is larger than Q. The large separation between Q and Q' suggests that the charged biexciton emission occurs at a larger momentum value compared with the emitting bright trion, indicating that the final state of the charged biexciton emission must be filled up to a momentum $\hbar Q'$ ($> \hbar Q$). This, in turn, suggests that the final state of charged biexciton emission is a dark trion ($\chi_D{}^-$), since the states in the bright trion band are empty for momentum $> \hbar Q$, and thus should have allowed transitions for momentum just above $\hbar Q$ (and hence, Q' should have been close to Q). Hence, it is instructive to consider that the charged biexciton is formed from a bright exciton and a dark trion (χ_D^-). The long-lived nature of the χ_D^- [38–40] keeps the band filled up to a momentum $\hbar Q'(> \hbar Q)$. Such a charged biexciton configuration with χ_D^- and χ^0 is in agreement with previous reports [36,41].

The zoomed-in version of the PL color plot in Fig. 1(d) (lines to guide the eye are drawn in yellow and red to represent the χ^- and β^- peak position, respectively) exhibits a striking "anticrossing"-like feature: the two peaks initially come close to each other, followed by a repulsion. Due to a large difference in the curvature between the initial and final states of the χ^- emission, the spectral redshift of this peak is initially much larger compared with the β^- peak [see Figs. 2(a) and 2(b)]. This effect, coupled with a gate field induced blueshift of the β^- peak, causes these two peaks to come closer at lower V_g. However, when V_g increases, the conduction-band filling slows down as the electrons start forming the long-lived dark trions [shown by a shaded curved arrow between Figs. 2(a) and 2(b)]. This, on the one hand, slows down the spectral movement of the χ^- peak, while on the other hand it enhances the spectral redshift of the β^- emission peak—forcing a spectral repulsion between the two peaks. This results in a V_g-dependent tunable spectral overlap between the χ^- and β^- peaks.

The PL spectra of some representative V_g values, along with the fitting of individual peaks (shaded area), are shown

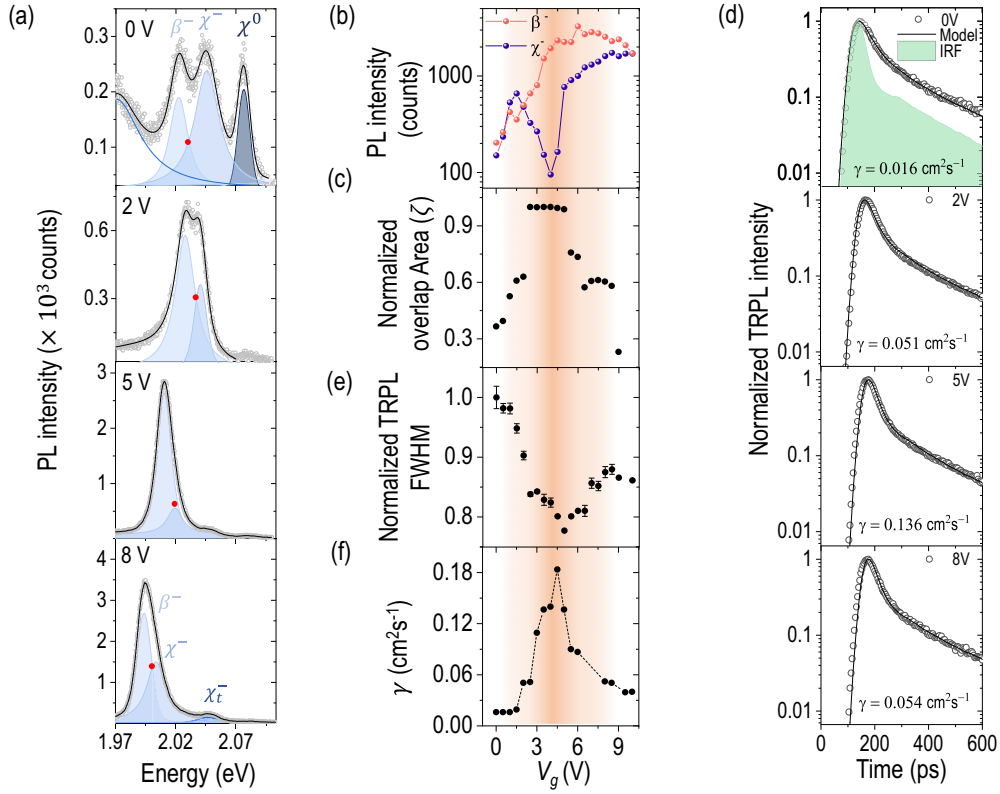

FIG. 3. Evidence of Auger induced trion-trion annihilation. (a) PL peak evolution for a few representative V_g values. The PL spectra and the corresponding fittings of individual peaks are shown by solid lines and shaded areas, respectively. At $V_g = 5$ V, almost complete overlap between χ^- and β^- is observed, coupled with a strong suppression of χ^- peak intensity. (b) PL intensity values of the fitted χ^- (blue spheres) and β^- (red spheres) peaks as a function of V_g. The shaded region indicates the strong Auger regime. (c) Spectral area overlap of χ^- and β^-, normalized with respect to χ^- area, is plotted with increasing V_g. The striking anticorrelation with the χ^- peak intensity in (b) is conspicuous in the strong Auger region. (d) TRPL data (open symbols) is fitted with Eq. (5) (solid traces) after deconvolution with the IRF, at representative V_g values. IRF is shown by the light blue shaded area for $V_g = 0$ V. (e) Normalized TRPL full width at half-maxima (FWHM) is plotted with respect to V_g, indicating a nonmonotonic trend with a reduced value in the strong Auger region. (f) Fitted values of the Auger coefficient (γ) from (d) are plotted with V_g, again showing nonmonotonic variation. The deep shaded region covering (b), (c), (e), and (f) represents the dominant Auger effect, which gradually reduces on both sides.

in Fig. 3(a). The variation of the PL intensity of the χ^- and β^- peaks as a function of V_g is shown in Fig. 3(b). We plot the corresponding spectral overlap (ζ) between the χ^- and β^- peaks (calculated as the overlap area between the two peaks normalized by the area under the χ^- peak) in Fig. 3(c) (after spectral overlap, fitting with a single peak and total peak FWHM are shown in Supplemental Material [24], Figs. 6 and 7, respectively). It is striking to note that the χ^- peak intensity is highly nonmonotonic with V_g. In particular, after an initial increase ($V_g \leqslant 1.5$ V), there is an anomalous suppression in the χ^- peak intensity with an increase in V_g in the range of $1.5 \leqslant V_g \leqslant 5$ V (shaded region), beyond which it again increases strongly. Comparing Figs. 3(b) and 3(c) reveals that the χ^- peak intensity has a strong negative correlation with ζ.

Further, we observe no such anomalous decrease in trion intensity when we excite the same sample with a continuous-wave laser (532 nm) at a power of 8.04 μW (see Supplemental Material [24], Fig. 8, for more details). The excitation density is ($\approx 4 \times 10^3$)-fold enhanced in the pulsed excitation mode compared with the continuous-wave case.

These observations directly indicate the role of TTA in the anomalous suppression of the trion emission intensity. The mechanism is explained in Fig. 4(a) (top panel). The measured photon energy $\hbar\omega$ ($\hbar\omega'$) of the χ^- (β^-) emission peak corresponds to the transitions between the states $|\chi^-\rangle$ and $|\mathrm{CB}\rangle$ ($|\beta^-\rangle$ and $|\chi_D^-\rangle$). When the spectral overlap is large, there is a strong resonance between these two transitions. Accordingly, at high excitation density, a bright trion (with COM $\hbar Q$) can undergo nonradiative recombination to the conduction band, providing its recombination energy to a dark trion (with COM momentum $\hbar Q'$). This receiving dark trion, with this energy, moves to the β^- state (with COM momentum $\hbar Q'$) due to the presence of the strong resonance between these two transitions. The β^- eventually emits a photon and relaxes back to the χ_D^- state. The net result of this entire process is the annihilation of a bright trion and the transfer of its oscillator strength for the formation of a charged biexciton. Such an Auger-induced TTA process efficiently suppresses the bright trion emission intensity in the range of $1.5 \leqslant V_g \leqslant 5$ V [shaded region in Figs. 3(a) and 3(b)]. However, when the spectral overlap between β^- and χ^- decreases ($V_g > 5$ V),

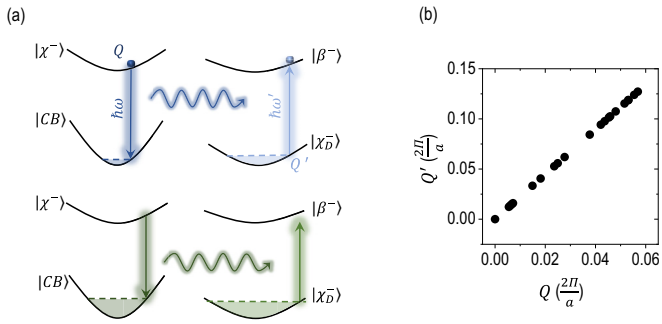

FIG. 4. Schematic diagram depicting the resonant Auger mechanism. (a) Schematic representation of the Auger interaction between two trions (χ^- and χ_D^-). When the spectral overlap between the β^- and χ^- transition is strong, the nonradiative annihilation of a χ^- gives rise to the transition of one χ_D^- to β^- state (top panel). When the spectral overlap is reduced, such strong resonance is eliminated, suppressing the Auger efficiency (bottom panel). (b) COM momentum for β^- (Q') is plotted with respect to that of χ^- (Q), obtained from Eq. (3). The energy corresponds to the maximum overlap point, indicated by the red dots in Fig. 3(a).

the transition from $|\chi_D^-\rangle$ to $|\beta^-\rangle$ state is less efficient due to breaking of the resonance, as depicted in Fig. 4(a) (lower panel).

Energy and linear momentum conservation during the Auger process provides the following relation between the momenta of the participating trion and biexciton:

$$Q'^2(V_g) = -\frac{15m_0}{2\hbar^2}\delta(V_g = 0) + 5Q^2(V_g), \tag{3}$$

where $\delta = \hbar(\omega - \omega')$. We assume that the effective mass for the electron and hole is $0.5m_0$ each. Using the maximum overlap energy value [indicated by the red dots in Fig. 3(a)] as the representative points for the Auger process, the relation between Q and Q' (corresponding to different V_g) is depicted in Fig. 4(b).

As stated before, when the spectral resonance reduces ($V_g > 5$ V), TTA is gradually suppressed, and χ^- peak intensity increases with V_g, as usual [Fig. 3(b)]. We also note that, after $V_g > 6$ V (when ζ is small), the β^- peak intensity reduces with an increase in V_g, which could be due to a lower generation of charged biexciton from the dark trion due to the suppressed Auger process.

To support the above-mentioned TTA mechanism, we perform *in situ* TRPL measurement on the sample (see the Methods section for experimental details). The raw time-resolved spectra are provided in Fig. 3(d) (open symbols) at representative V_g values. In Fig. 3(e), we plot the extracted (normalized) full width at half-maximum (FWHM) of the decay plot, which indicates a faster decay in the regime where the trion intensity is suppressed. The observation of a faster decay of the trion at larger spectral overlap, coupled with reduced emission intensity, suggests an increasingly faster nonradiative process, supporting the TTA mechanism. At larger V_g (>5 V), when the spectral overlap is smaller, TTA is suppressed, leading to an increase in the FWHM of the decay plot [Fig. 3(e)].

The decay of the time-dependent bright trion population density [$n(t)$] at Q is given by

$$\frac{dn(t)}{dt} = -\frac{n(t)}{\tau} - \gamma n(t) n_d(t). \tag{4}$$

Here, τ is the trion decay timescale, which includes both radiative and nonradiative mechanisms (other than TTA), while γ is the Auger coefficient for the TTA process. $n(t)$ and $n_d(t)$ are the bright and dark trion population density at Q and Q', respectively. Note that both the bright and dark trion bands have similar curvature. Given that we are considering a two-dimensional system, the density of states is independent of the momentum. Thus, both bands have a similar density of states irrespective of the values of Q and Q'. In addition, we also expect that at these momentum values, the filling factors are similar since trion and biexciton radiative recombination peaks around Q and Q', respectively. Hence, we approximate $n_d(t) \approx n(t)$. Then $n(t)$ can be written as

$$n(t) = \frac{n(0)e^{-t/\tau}}{1 + [n(0)\gamma\tau](1 - e^{-t/\tau})}. \tag{5}$$

$n(0)$ is the trion population at time $t = 0$, and is estimated to be $\sim 10^{12}$ cm^{-2} at the given laser power. Finally, the experimental TRPL spectra are fitted with

$$n'(t) = n(t) + \beta_1 e^{-t/\tau_1} + \beta_2 e^{-t/\tau_2} \tag{6}$$

by deconvoluting with the instrument response function (IRF). The second and third terms, respectively, take into account the decay from the charged biexciton and small defect tail in the spectral overlapping region. We use γ, β_1, and β_2 as fitting parameters. The respective values of τ, τ_1, and τ_2 are obtained from the non-TTA region (that is, $V_g < 0$ V) and kept as constant at $\tau = 14$ ps, $\tau_1 = 50$ ps, and $\tau_2 = 750$ ps [see Supplemental Material [24], Figs. 9(a) and 9(b), for details]. These obtained lifetime values for trion and charged biexciton agree well with existing reports [39,42,43]. The obtained fittings of the experimental data in the TTA region with Eq. (6) are shown as the solid traces in Fig. 3(d). The value of γ ensuring the best fit with the experimental data is plotted in Fig. 3(f) at different gate voltages.

It is clear from Fig. 3(f) that γ is a strong function of V_g induced spectral overlap between χ^- and β^-. In particular, we extract $\gamma = 0.016$ cm^2 s^{-1} at small positive V_g, which increases by about ten-fold to $\gamma = 0.18$ cm^2 s^{-1} at $V_g = 4.5$ V. This suggests that the spectral overlap between the two transition energies [Fig. 4(a)] is essential to enhance the TTA process.

In conclusion, we demonstrate a large tunability of charged exciton and charged biexciton spectral features by applying a gate voltage. This allows us to directly map the large center-of-mass momentum associated with these emitting species, in stark contrast to the zero-momentum neutral exciton. When the two charged species are close to spectral resonance, we observe an anomalous suppression of the bright trion intensity with increasing gate voltage, suggesting a trion-trion annihilation through the Auger process facilitated by the spectral resonance. We could tune the strength of the Auger process ten-fold by varying the gate-voltage-dependent spectral overlap. Such an electrically tunable resonant Auger process could

be a prospective tool to explore more complex many-body phenomena among higher-order excitonic complexes.

III. METHODS

Sample preparation. The top-gated stack is prepared by mechanical exfoliation of the individual layers from bulk crystals of WS_2, hBN, and graphite. First, the exfoliation is performed on polydimethylsiloxane (PDMS) using 3M^{TM} scotch tape, and then the layers are transferred sequentially onto Si substrate covered with 285-nm-thick SiO_2. The few-layer graphene layers for the top gate electrode and the grounding electrode are connected to two different prepatterned metal pads. The metal pads are fabricated using direct laser lithography, followed by sputtering of Ni/Au (10/50 nm) and liftoff. The deterministic transfer process is performed at room temperature under an optical microscope using a micromanipulator. After the transfer process is complete, the stack is annealed at 200 °C for 3 h in a high vacuum chamber (10^{-6} mbar) to ensure better adhesion between layers.

Sample characterization. A pulsed laser head of 531 nm wavelength (PicoQuant) operated by a PDL-800D laser driver is used for optical excitation. The laser has a pulse width of 48 ps with a variable repetition rate (10 MHz is used in this work). A 50:50 beam splitter is used to divert half of the emission signal from the sample (see Fig. 1 in Supplemental Material for a schematic) to a spectrometer for steady-state PL. The other half of the emission signal is directed to a single photon avalanche detector (SPD-050-CTC from Micro Photon Devices). The detector is connected to a Time-Correlated Single Photon Counting (TCSPC) system (PicoHarp 300 from PicoQuant). The time-resolved dynamics of the trion is obtained using a 610 nm bandpass filter (FWHM 10 nm) before the single-photon detector. The setup's instrument response function (IRF) has a decay of ∼23 ps and an FWHM of ∼52 ps.

ACKNOWLEDGMENTS

This work was supported in part by a Core Research Grant from the Science and Engineering Research Board (SERB) under Department of Science and Technology (DST), a grant from Indian Space Research Organization (ISRO), a grant from MHRD under STARS, and a grant from MHRD, MeitY, and DST Nano Mission through NNetRA. K.W. and T.T. acknowledge support from the Elemental Strategy Initiative conducted by the MEXT, Japan (Grant Number JPMXP0112101001) and JSPS KAKENHI (Grant Numbers 19H05790, 20H00354 and 21H05233).

The authors declare no competing financial or nonfinancial interests.

[1] K. F. Mak, K. He, C. Lee, G. H. Lee, J. Hone, T. F. Heinz, and J. Shan, Tightly bound trions in monolayer MoS_2, Nat. Mater. **12**, 207 (2013).

[2] J. S. Ross, S. Wu, H. Yu, N. J. Ghimire, A. M. Jones, G. Aivazian, J. Yan, D. G. Mandrus, D. Xiao, W. Yao *et al.*, Electrical control of neutral and charged excitons in a monolayer semiconductor, Nat. Commun. **4**, 1474 (2013).

[3] A. Singh, G. Moody, K. Tran, M. E. Scott, V. Overbeck, G. Berghäuser, J. Schaibley, E. J. Seifert, D. Pleskot, N. M. Gabor, J. Yan, D. G. Mandrus, M. Richter, E. Malic, X. Xu, and X. Li, Trion formation dynamics in monolayer transition metal dichalcogenides, Phys. Rev. B **93**, 041401(R) (2016).

[4] Y. You, X.-X. Zhang, T. C. Berkelbach, M. S. Hybertsen, D. R. Reichman, and T. F. Heinz, Observation of biexcitons in monolayer WSe_2, Nat. Phys. **11**, 477 (2015).

[5] Z. Ye, L. Waldecker, E. Y. Ma, D. Rhodes, A. Antony, B. Kim, X.-X. Zhang, M. Deng, Y. Jiang, Z. Lu *et al.*, Efficient generation of neutral and charged biexcitons in encapsulated WSe_2 monolayers, Nat. Commun. **9**, 3718 (2018).

[6] C. Robert, T. Amand, F. Cadiz, D. Lagarde, E. Courtade, M. Manca, T. Taniguchi, K. Watanabe, B. Urbaszek, and X. Marie, Fine structure and lifetime of dark excitons in transition metal dichalcogenide monolayers, Phys. Rev. B **96**, 155423 (2017).

[7] S.-Y. Chen, T. Goldstein, T. Taniguchi, K. Watanabe, and J. Yan, Coulomb-bound four-and five-particle intervalley states in an atomically-thin semiconductor, Nat. Commun. **9**, 3717 (2018).

[8] S. Chatterjee, S. Das, G. Gupta, K. Watanabe, T. Taniguchi, and K. Majumdar, Probing biexciton in monolayer WS_2 through controlled many-body interaction, 2D Mater. **9**, 015023 (2021).

[9] M. Paur, A. J. Molina-Mendoza, R. Bratschitsch, K. Watanabe, T. Taniguchi, and T. Mueller, Electroluminescence from multi-particle exciton complexes in transition metal dichalcogenide semiconductors, Nat. Commun. **10**, 1709 (2019).

[10] D. Erkensten, S. Brem, and E. Malic, Exciton-exciton interaction in transition metal dichalcogenide monolayers and van der waals heterostructures, Phys. Rev. B **103**, 045426 (2021).

[11] D. F. Cordovilla Leon, Z. Li, S. W. Jang, and P. B. Deotare, Hot exciton transport in WSe_2 monolayers, Phys. Rev. B **100**, 241401(R) (2019).

[12] E. Linardy, D. Yadav, D. Vella, I. A. Verzhbitskiy, K. Watanabe, T. Taniguchi, F. Pauly, M. Trushin, and G. Eda, Harnessing exciton-exciton annihilation in two-dimensional semiconductors, Nano Lett. **20**, 1647 (2020).

[13] C. M. E. Chow, H. Yu, J. R. Schaibley, P. Rivera, J. Finney, J. Yan, D. Mandrus, T. Taniguchi, K. Watanabe, W. Yao *et al.*, Monolayer semiconductor auger detector, Nano Lett. **20**, 5538 (2020).

[14] P. D. Cunningham, K. M. McCreary, and B. T. Jonker, Auger recombination in chemical vapor deposition-grown monolayer WS_2, J. Phys. Chem. Lett. **7**, 5242 (2016).

[15] A. Singh, G. Moody, S. Wu, Y. Wu, N. J. Ghimire, J. Yan, D. G. Mandrus, X. Xu, and X. Li, Coherent Electronic Coupling in Atomically Thin $MoSe_2$, Phys. Rev. Lett. **112**, 216804 (2014).

[16] Y. Hoshi, T. Kuroda, M. Okada, R. Moriya, S. Masubuchi, K. Watanabe, T. Taniguchi, R. Kitaura, and T. Machida, Suppression of exciton-exciton annihilation in tungsten disulfide monolayers encapsulated by hexagonal boron nitrides, Phys. Rev. B **95**, 241403(R) (2017).

[17] D. Sun, Y. Rao, G. A. Reider, G. Chen, Y. You, L. Brézin, A. R. Harutyunyan, and T. F. Heinz, Observation of rapid exciton-exciton annihilation in monolayer molybdenum disulfide, Nano Lett. **14**, 5625 (2014).

[18] Y. Lee, T. T. Tran, Y. Kim, S. Roy, T. Taniguchi, K. Watanabe, J. I. Jang, and J. Kim, Enhanced radiative exciton recombination in monolayer WS_2 on the hbn substrate competing with nonradiative exciton–exciton annihilation, ACS Photon. **9**, 873 (2022).

[19] O. Salehzadeh, N. Tran, X. Liu, I. Shih, and Z. Mi, Exciton kinetics, quantum efficiency, and efficiency droop of monolayer MoS_2 light-emitting devices, Nano Lett. **14**, 4125 (2014).

[20] E. Yablonovitch and T. Gmitter, Auger recombination in silicon at low carrier densities, Appl. Phys. Lett. **49**, 587 (1986).

[21] A. Beattie and P. Landsberg, Auger effect in semiconductors, Proc. R. Soc. London A **249**, 16 (1959).

[22] T. Kuroda, Y. Hoshi, S. Masubuchi, M. Okada, R. Kitaura, K. Watanabe, T. Taniguchi, and T. Machida, Dark-state impact on the exciton recombination of WS_2 monolayers as revealed by multi-timescale pump-probe spectroscopy, Phys. Rev. B **102**, 195407 (2020).

[23] Y.-S. Park, W. K. Bae, J. M. Pietryga, and V. I. Klimov, Auger recombination of biexcitons and negative and positive trions in individual quantum dots, ACS Nano **8**, 7288 (2014).

[24] See Supplemental Material at http://link.aps.org/supplemental/10.1103/PhysRevB.105.L121409. for additional details on the time-resolved and steady-state photoluminescence measurements.

[25] Z. Wang, L. Zhao, K. F. Mak, and J. Shan, Probing the spin-polarized electronic band structure in monolayer transition metal dichalcogenides by optical spectroscopy, Nano Lett. **17**, 740 (2017).

[26] M. Li, S. Biswas, C. U. Hail, and H. A. Atwater, Refractive index modulation in monolayer molybdenum diselenide, Nano Lett. **21**, 7602 (2021).

[27] D. Van Tuan, B. Scharf, I. Žutić, and H. Dery, Marrying Excitons and Plasmons in Monolayer Transition-Metal Dichalcogenides, Phys. Rev. X **7**, 041040 (2017).

[28] N. Abraham, K. Watanabe, T. Taniguchi, and K. Majumdar, Anomalous stark shift of excitonic complexes in monolayer WS_2, Phys. Rev. B **103**, 075430 (2021).

[29] S. Kallatt, S. Das, S. Chatterjee, and K. Majumdar, Interlayer charge transport controlled by exciton-trion coherent coupling, npj 2D Mater. Appl. **3**, 15 (2019).

[30] V. Huard, R. T. Cox, K. Saminadayar, A. Arnoult, and S. Tatarenko, Bound States in Optical Absorption of Semiconductor Quantum Wells Containing a Two-Dimensional Electron Gas, Phys. Rev. Lett. **84**, 187 (2000).

[31] B. Stébé and A. Ainane, Ground state energy and optical absorption of excitonic trions in two dimensional semiconductors, Superlatt. Microstruct. **5**, 545 (1989).

[32] K. Murali, M. Dandu, K. Watanabe, T. Taniguchi, and K. Majumdar, Accurate extraction of schottky barrier height and universality of fermi level de-pinning of van der waals contacts, Adv. Func. Mater. **31**, 2010513 (2021).

[33] S. Das, M. Dandu, G. Gupta, K. Murali, N. Abraham, S. Kallatt, K. Watanabe, T. Taniguchi, and K. Majumdar, Highly tunable layered exciton in bilayer WS_2: Linear quantum confined stark effect versus electrostatic doping, ACS Photon. **7**, 3386 (2020).

[34] F. Rana, O. Koksal, M. Jung, G. Shvets, and C. Manolatou, Many-body theory of radiative lifetimes of exciton-trion superposition states in doped two-dimensional materials, Phys. Rev. B **103**, 035424 (2021).

[35] K. Wagner, E. Wietek, J. D. Ziegler, M. A. Semina, T. Taniguchi, K. Watanabe, J. Zipfel, M. M. Glazov, and A. Chernikov, Autoionization and Dressing of Excited Excitons by Free Carriers in Monolayer WSe_2, Phys. Rev. Lett. **125**, 267401 (2020).

[36] M. Barbone, A. R.-P. Montblanch, D. M. Kara, C. Palacios-Berraquero, A. R. Cadore, D. De Fazio, B. Pingault, E. Mostaani, H. Li, B. Chen *et al.*, Charge-tuneable biexciton complexes in monolayer WSe_2, Nat. Commun. **9**, 3721 (2018).

[37] G. Gupta and K. Majumdar, Fundamental exciton linewidth broadening in monolayer transition metal dichalcogenides, Phys. Rev. B **99**, 085412 (2019).

[38] F. Volmer, S. Pissinger, M. Ersfeld, S. Kuhlen, C. Stampfer, and B. Beschoten, Intervalley dark trion states with spin lifetimes of 150 ns in WSe_2, Phys. Rev. B **95**, 235408 (2017).

[39] E. Liu, J. van Baren, Z. Lu, M. M. Altaiary, T. Taniguchi, K. Watanabe, D. Smirnov, and C. H. Lui, Gate Tunable Dark Trions in Monolayer WSe_2, Phys. Rev. Lett. **123**, 027401 (2019).

[40] Z. Li, T. Wang, Z. Lu, M. Khatoniar, Z. Lian, Y. Meng, M. Blei, T. Taniguchi, K. Watanabe, S. A. McGill *et al.*, Direct observation of gate-tunable dark trions in monolayer WSe_2, Nano Lett. **19**, 6886 (2019).

[41] M. Zinkiewicz, T. Woźniak, T. Kazimierczuk, P. Kapuscinski, K. Oreszczuk, M. Grzeszczyk, M. Bartoš, K. Nogajewski, K. Watanabe, T. Taniguchi *et al.*, Excitonic complexes in n-doped WS_2 monolayer, Nano Lett. **21**, 2519 (2021).

[42] G. Wang, L. Bouet, D. Lagarde, M. Vidal, A. Balocchi, T. Amand, X. Marie, and B. Urbaszek, Valley dynamics probed through charged and neutral exciton emission in monolayer WSe_2, Phys. Rev. B **90**, 075413 (2014).

[43] P. Nagler, M. V. Ballottin, A. A. Mitioglu, M. V. Durnev, T. Taniguchi, K. Watanabe, A. Chernikov, C. Schüller, M. M. Glazov, P. C. M. Christianen, and T. Korn, Zeeman Splitting and Inverted Polarization of Biexciton Emission in Monolayer WS_2, Phys. Rev. Lett. **121**, 057402 (2018).